Article

Rapid Water Quality Mapping from Imaging Spectroscopy with a Superpixel Approach to Bio-Optical Inversion

Nicholas R. Vaughn [1,*] **, Marcel König** [2] **, Kelly L. Hondula** [1] **, Dominica E. Harrison** [1] **and Gregory P. Asner** [1]

1   Center for Global Discovery and Conservation Science, Arizona State University, Hilo, HI 96720, USA; khondula@asu.edu (K.L.H.); deharri9@asu.edu (D.E.H.); gregasner@asu.edu (G.P.A.)
2   Brockmann Consult GmbH, 21029 Hamburg, Germany; marcel.koenig@brockmann-consult.de
*   Correspondence: nickvaughn@asu.edu

Abstract: High-resolution water quality maps derived from imaging spectroscopy provide valuable insights for environmental monitoring and management, but the processing of all pixels of large datasets is extremely computationally intensive and limits the speed of map production. We demonstrate a superpixel approach to accelerating water quality parameter inversion on such data to considerably reduce time and resource needs. Neighboring pixels were clustered into spectrally similar superpixels, and bio-optical inversions were performed at the superpixel level before a nearest-neighbor interpolation of the results back to pixel resolution. We tested the approach on five example airborne imaging spectroscopy datasets from Hawaiian coastal waters, comparing outputs to pixel-by-pixel inversions for three water quality parameters: suspended particulate matter, chlorophyll-a, and colored dissolved organic matter. We found significant reduction in computational time, ranging from 38 to 2625 times faster processing for superpixel sizes of 50 to 5000 pixels (200 to 20,000 m^2). Using 1000 paired output values from each example image, we found minimal reduction in accuracy (as decrease in R^2 or increase in RMSE) of the model results when the superpixel size was less than 750 2 m × 2 m resolution pixels. Such results mean that this methodology could reduce the time needed to produce regional- or global-scale maps and thereby allow environmental managers and other stakeholders to more rapidly understand and respond to changing water quality conditions.

Keywords: pollution; turbidity; sedimentation; conservation; Hawai'i; Global Airborne Observatory

1. Introduction

Monitoring of changes in water quality is extremely important for understanding and responding to events that can affect human and ecosystem health [1]. To this end, remote-sensing technology has revolutionized our ability to monitor water quality at large spatial scales by reducing time spent in the field sampling and at the same time drastically increasing the spatial sampling frequency [2]. Maps of water quality produced from remote-sensing data allow wall-to-wall coverage of a region of interest with high enough spatial resolution to discern distributional patterns in individual water quality parameters. Maps with such high spatial detail allow researchers and environmental managers to better track changes in water bodies over time, identify pollution sources and hotspots, and implement targeted conservation strategies [2–4]. The development of remote-sensing-based water-quality-mapping capability has progressed along with the development in the spatial resolution and spectral fidelity of the available sensors.

One rapidly developing technology that has greatly improved our ability to map water quality parameters of interest is imaging spectroscopy, which measures reflected solar radiation sampled across a large number of spectral bands at increasingly fine spectral and spatial resolutions [5,6]. Unlike multispectral instruments, which are more limited to empirical fitting of band ratios to individual water quality parameters (see [7] for several examples), the expanded spectral detail provided by imaging spectroscopy allows for the

simultaneous detection and quantification of various water quality parameters, including chlorophyll-a (Chl-a), suspended particulate matter (SPM), and colored dissolved organic matter absorbption coefficient at 440nm (CDOM) [6,8,9]. A common approach to this problem is to use optimization techniques applied to iterative forward simulations of radiative transfer through the water body using a radiative transfer model with adjustable parameters for bottom reflectance and water properties [10].

When it comes to responding to water quality issues involving human or ecosystem health, time is of the utmost importance. While water quality mapping from imaging spectrometer data yields improvements in accuracy over simpler data types, the process is extremely complex and time-consuming. Indeed, data latency is one of the key factors hindering the adoption of remote-sensing technology into water quality management practices [11]. In addition to modeling out the effects of an air atmosphere, methods for retrieving water quality information from spectrometer data typically require modeling the radiative transfer of light through a column of water, involving a very large number of unknowns [12–16], and unmixing the influence of water properties and the bottom surface quickly becomes a very lengthy and underdetermined computation, even for modern computing architectures [17]. More rapid approaches use empirical models based on band ratios and indices; however, these approaches require re-calibration and cannot be quickly adapted to new regions of interest and likely even different coverage dates [18]. The high spatial and spectral resolutions of modern imaging spectroscopy datasets afford millions or even billions of individual reflectance spectra needing to be fit. Even with cluster computers, this extreme number can present a significant hurdle when trying to build large-scale water quality maps from such data on short time scales. Techniques to speed up this modeling can make mapping projects much more tractable and, more importantly, increase the speed at which useful maps of water quality can be made available to rapidly detect and respond to significant changes in water quality.

Here, we develop and demonstrate a working approach for accelerating water quality parameter inversion on large imaging spectroscopy datasets to overcome the computational challenges that hinder our ability to meet these rapid, actionable mapping needs. This approach utilizes two key features to achieve significantly reduced computational time with minimal loss of accuracy. First, neighboring pixels of the input reflectance map are clustered into superpixels, or clusters of neighboring and spectrally similar pixels. Spectra from the pixels within these superpixel clusters are averaged and inversions are performed at the superpixel level. Second, these model-fitting results are then back-interpolated to all original pixels using a local regression model. We describe this algorithm in detail and answer the following questions to determine if this approach is useful. First, how closely do outputs from the algorithm match computational gains and accuracy losses from using this approach over the pixel-by-pixel approach on some sample datasets? Second, what levels of efficiency gains can be achieved? Finally, because the superpixel size should affect both answers above, is there an optimal spatial scale for the superpixels to maximize the utility and accuracy of this algorithm?

2. Materials and Methods

2.1. Bio-Optical Inversion Model

For this investigation, we used the bio_optics package version 0.0.2 [19] for the inversion of three individual water quality parameters, Chl-a (μgL^{-1}), SPM (mgL^{-1}), and CDOM (m^{-1}). This package contains an inversion optimization tool that incorporates the bio-optical simulation model of Albert and Mobley [13] and the water surface reflectance model of Gege [20]. For inversion, we used the default input parameters (mostly provided as part of the water color simulator software package WASI version 6 [15]) to compute the spectral absorption and backscattering of the water body.

Bottom reflectance is simulated as a mixture of endmembers representing different benthic cover classes. To better match the model results to the study region, we used a

custom bottom reflectance (R_b) library with four benthic classes, (1) sand, (2) live coral, (3) algae, and (4) dark rock, built using averaged example in situ spectra collected locally.

The inversion window included 54 spectral bands between the wavelengths 420 to 690 nm. During optimization, the mean absolute error—calculated as the sum of all band-wise absolute differences between observed and simulated below-surface remote sensing—was used as a loss function. Parameters allowed to vary during model optimization included the following (see [19] for details):

- Concentrations of Chl-a in μgL^{-1} from 6 different phytoplankton types (C_0 through C_5), all with a starting value of 0.1 and an allowed range of 0.0 to 100.0;
- The concentration of Mie-scattering particles (C_{Mie}) in mgL^{-1}, with a starting value of 0.1 and an allowed range of 0.0 to 100.0;
- The concentration of particles with a spectrally flat backscattering response (C_X) in mgL^{-1}, with a starting value of 0.5 and an allowed range of 0.0 to 100.0;
- The CDOM absorption coefficient at wavelength 440 nm (C_Y) in m^{-1} units, with a starting value of 0.01 and an allowed range of 0.00 to 4.00;
- Contributions of each of the four benthic cover classes to bottom reflectance (f_1 through f_4), each with a starting value of 0.25 and an allowed range of 0.00 to 1.00;
- Water depth (z_B) in meters, with a starting value of 10.0 and an allowed range of 0.0 to 100.0;
- Surface glint, using the intensity of direct glint (g_{dd}) as well as diffuse glint originating from Raleigh and aerosol scattering processes (g_{dsr} and g_{dsa}).

After inversion, the three parameters of interest were retrieved from the fitted parameters using the following equations:

$$Chl\text{-}a = \sum_{i \in [0,5]} C_i \tag{1}$$

$$CDOM = C_Y \tag{2}$$

$$SPM = C_X + C_{MIE} + \frac{Chl\text{-}a}{1000} \tag{3}$$

2.2. Validation Data

To test our algorithm, we chose five individual flight lines of reflectance imagery collected by the Global Airborne Observatory (GAO) [21] from example sites across the Hawaiian Islands (Table 1). Each of these test images exhibited easily identifiable gradients of one or more of the water quality parameters of interest. The GAO VSWIR spectrometer measures radiance in 428 calibrated channels ranging from 348 to 2486 nm at approximately 5 nm intervals, with the full width half max for each channel ranging from 5.49 to 5.82 nm. The instrument is radiometrically calibrated on the ground using an integration sphere and standard NIST lighting instrumentation at least once a year to update the individual band center wavelengths, compute correction factors for uniformity of detector elements, and compute the coefficients used to convert raw digital number values into calibrated radiance readings ($\mu Wcm^{-2}Sr^{-1}nm^{-1}$). The pushbroom instrument has a field of view of 34 degrees, which measures cross-track in 598 samples at a rate of 100 Hz.

During collection for all of the above flight lines, nominal altitude was 2000 m above ground level with a maximum air speed of approximately 130 kts ($66.9 \, ms^{-1}$), which, when orthorectified, results in a spatial resolution of 2×2 m. Days and times of data collection were tightly managed to minimized variation in solar lighting and water surface conditions. To manage lighting conditions and solar glint, we targeted sections of coastline with clear skies and limited data collection to the hours 9 AM to 11:30 AM, and the aircraft azimuth was set such that the sun was behind the tail of the aircraft to manage solar angles. If winds were picked up before 11:30, then another location was targeted or data collection was stopped so that we could minimize water surface variations to further minimize solar glint.

Table 1. Information on the five imaging spectroscopy datasets used as the validation of the proposed algorithm. All times are in 24 h format, and Latitude and Longitude are in decimal degrees.

Site	Name	Date	Local Time	Latitude	Longitude
1	Pelekane Bay	30 October 2023	10:02	20.0243	−155.8256
2	East Kahoʻolawe	22 January 2024	09:15	20.6027	−156.5638
3	Hilo Bay	15 January 2023	11:30	19.7353	−155.0636
4	Māʻalaea Bay	22 January 2024	10:19	20.7805	−156.4842
5	South Molokaʻi	7 January 2024	11:31	21.0866	−157.2159

We transformed calibrated radiance data from each of the test sites above into above-surface reflectance (R, unitless) using the "apply_oe" tool provided in the ISOFIT package [22,23] version 2.10.2. During this processing, each image was broken into clusters representing approximately 1600 m^2 of area on the Earth's surface (approx. 400 image pixels), and atmospheric correction was applied to each of these clusters to obtain a posterior estimate of reflectance. For this, we used an empirically derived prior surface covariance model that was computed by ISOFIT from a library of ocean and terrestrial reflectance spectra collected for the PRISM mission. The cluster-level inversions were then used in an empirical line approach to create a linear model of radiance to reflectance for each band, which could be applied to the individual pixel radiance spectra from the image to create a map of modeled reflectance scaled as a value from 0 to 1.

The resulting reflectance images were next processed using a series of multi-band indices used as filters to mask out pixels representing non-water surfaces, crashing waves, shadowed bottom surface conditions, and extreme amounts of direct solar glint. Any pixel failing one or more of the following tests of water reflectance patterns was removed from consideration in the water quality mapping:

1. An Automated Water Extraction Index [24] greater than 0.005;
2. A Modified Normalized Difference Water Index [25] greater than 0.2;
3. An NIR glint metric, computed as the mean reflectance of all bands between 880 and 920 nm, less than 0.06;
4. A brightness metric, computed as the mean reflectance of all bands between 500 and 560 nm, greater than 0.01;
5. A green–nir slope metric, computed as the negative of the slope parameter of a regression line fit to reflectance values for all bands between 575 and 700 nm against the center wavelengths of these bands, divided by the value of the glint metric in (3) above, greater than 0.0025;
6. The same brightness metric as in (4) above less than 0.15 OR a blue-green slope index, computed as (reflectance at 490 nm − reflectance at 440 nm)/(reflectance at 440 nm), greater than 0.05.

Tests 1 and 2 were quick to separate terrestrial and aquatic reflectance spectra. The glint metric (3) easily identified pixels where any below-surface spectral signal would be lost in the high noise of solar glint after glint removal. The minimum brightness score (4) detected pixels where shadowing on the bottom surface drastically reduced the signal-to-noise ratio. With initial tests using a simple filter of high brightness, we found that a bright sand bottom surface could lead to similar levels of brightness as aerated water near crashing waves. Tests 5 and 6 were developed to better separate these two cases and enable masking of the latter. After masking pixels that were not appropriate for inversion modeling, we converted the remaining reflectance spectra R into above-surface radiance reflectance (r_{rs0+}; sr^{-1}), used as input by the inversion model, by dividing all bands by π. The glint signal remaining in the r_{rs0+} spectra would later be modeled out during the inversion modeling.

2.3. The Superpixel Approach

To greatly speed up the time it takes to produce a high-resolution map of water quality parameters from a single flight line of airborne imaging spectrometer data, our algorithm started with the creation of superpixels from the input dataset (Figure 1). In the first step, water pixels in the input surface reflectance image were segmented into superpixels. Because these superpixels have similar spectral characteristics, they can be treated as a meaningful sampling unit if within-superpixel variance is significantly smaller than between-superpixel variance. While there are several superpixel clustering algorithms to break each of the non-orthorectified spectral images into superpixels [26], we chose the SLIC algorithm [27] because it is well tested, sufficiently fast, and easily implemented using the Scikit-Image python package [28]. This algorithm has also been demonstrated successfully on water color data [29].

In brief, the SLIC algorithm begins by evenly spreading cluster center points across the image. A smoothing operation, controlled by a sigma value, is applied to the image. Then, each cluster is given the X, Y location and the spectral color values of the nearest pixel. Each pixel is then assigned to the cluster with the closest (Euclidean) values for both X, Y location and pixel color, weighted by a compactness parameter that affects the relative scaling of location versus color values (higher compactness will more greatly emphasize location differences over color differences, keeping the clusters more uniformly shaped). Once all pixels are assigned, the cluster centers and color are recomputed from the average of all pixels within the clusters. Pixel assignment and cluster mean computation are repeated iteratively until centers are stable, and a 2-dimensional image array is returned with each pixel valued as an integer cluster ID. In this paper, the resulting clusters were used as superpixels.

Superpixel clustering was performed using all spectral bands within the model-fitting range of 420 to 690 nm. For this approach, we adjusted two parameters of the SLIC function: (1) We used a compactness parameter of 0.1 to allow the superpixel shapes to better follow natural edges in water quality parameter distribution resulting from water eddies and currents. (2) We used a sigma value of 2.0 for the smoothing operation of the SLIC algorithm to reduce the impact of spectral noise on superpixel determination. However, we found that these parameters worked well for 2 m resolution data, and these parameters might need adjustment for different image resolutions.

The water quality parameter inversion, the slowest step by far, was then performed at the superpixel level. The bio-optical model described above was used to obtain estimates of the three water quality parameters from the average reflectance spectrum of each superpixel. This was also a chance to run quality control on the bio-optical model outputs and ignore superpixels when bio-optical model outputs were less certain. Superpixels for which the model did not reach an optimal solution within the 400 allowed iterations were removed from further consideration.

Next, the superpixel-level water quality parameters were back-interpolated from superpixels into the original pixel resolution. This was performed using a nearest-neighbor approach where the individual pixels were matched to spectrally similar superpixels. For this, we reduced the dimensionality and noise by performing a principal component analysis (PCA) on brightness-normalized average reflectance spectra from the superpixels. The rotations from the first six orthogonal components of the PCA were applied to both the superpixel reflectance data and the pixel reflectance data. Then, for each pixel, water quality values were computed using inverse-distance weighted averages of water quality values from the *k* nearest superpixel neighbors in six-dimension PCA space. After comparing different values, we determined that a *k* of 4 balanced the contradicting desires to increase stability of results and to avoid excessive smoothing of the resulting maps.
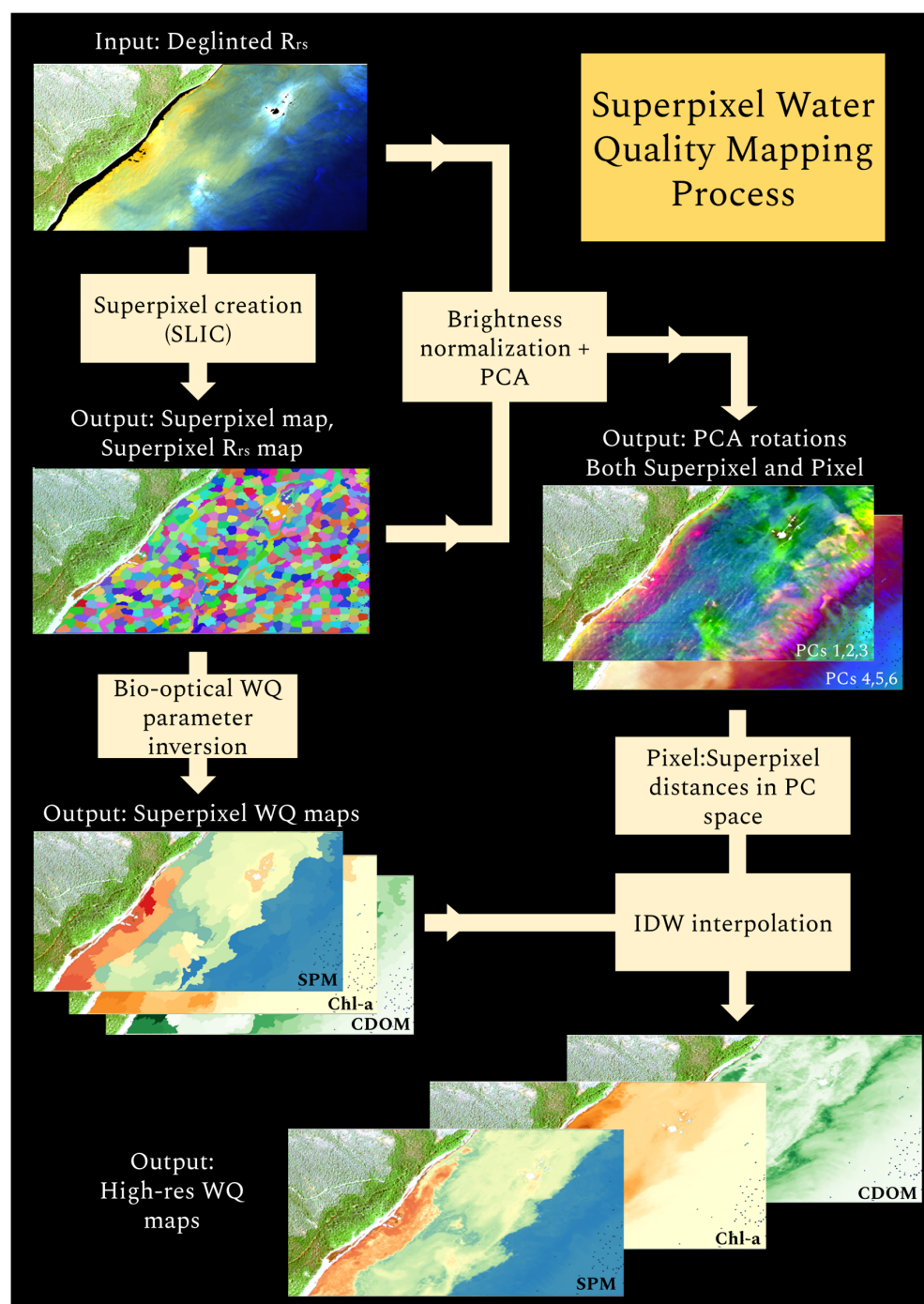
Figure 1. The superpixel water-quality-mapping process for decreasing time and computational needs for high-resolution output maps of suspended particulate matter (SPM), chlorophyll-a (Chl-a), and colored dissolved organic matter (CDOM).

2.4. Analysis

For each of the example reflectance images, we ran the bio-optical model both on a pixel-by-pixel basis and using the superpixel approach defined above. We ran the super-pixel approach using a single processor core for each flight line in our study, and we kept track of the full time needed for the process to be complete for each example site reflectance image. For the pixel-by-pixel approach, we processed all pixels on a computing cluster [30] in parallel chunks of three rows. Beyond the inversions, the only other time-consuming step of the pixel-by-pixel approach was reflectance map input and water quality map out-

put. To obtain a comparable estimate of the time needed for the pixel-by-pixel approach on a single core, we multiplied the number of pixels by the average time for spectral inversion plus 0.0001 s per pixel for file input and output.

To test the effect of superpixel size on the speed and quality of output water quality maps, we ran the superpixel approach for five example sites using 13 different superpixel size settings: 50, 100, 250, 500, 600 (default superpixel size), 750, 1000, 1250, 1500, 2000, 3000, 4000, and 5000 pixels. We tracked similarity in the output maps using both horizontal transect profiles for visualization and regression models applied to matching pixels for 1000 randomly selected water pixels within each location. R^2 and RMSE values were collected and used to directly compare approaches and settings for the same reflectance image.

We also assessed variation in the output maps from the pixel-by-pixel approach within the SLIC individual clusters identified in the superpixel approach across the various superpixel size settings. Total variance (SST) was computed as the sum of squared differences between pixel values and the mean value across the entire map. After computing the mean values for each SLIC cluster, we computed error variance (SSE) as the sum of all squared differences between pixel values and their associated cluster mean. RMSE was computed by dividing the SSE by the total number of valid pixels in each map and taking the square root of the resulting value. The proportion of variance explained by within-cluster error was computed as SSE/SST. By performing this analysis at each superpixel size setting, we could assess how well the cluster sizes match the scales of variation in the water quality variables across the five example sites.

3. Results

With an iteration limit of 400 on the inversion optimization process, we found that the average number of seconds per inversion was 3.877 across many thousands of inversions completed in this project. Across the different example sites, using the default nominal superpixel size of 600 pixels (2400 m^2 of surface coverage), we found that the superpixel approach to bio-optical inversion sped up map production from 218.8 to 511.5 times versus a pixel-by-pixel approach (Table 2). There was no noticeable correlation between this increase in speed and the number of valid water pixels in the reflectance map.

Table 2. Computational requirement information about the pixel-by-pixel approach and the superpixel approach for each example site using a superpixel size of 600. The Pixels column specifies the number of remaining water pixels after the filtering described in Section 2.2.

Site	Name	Pixels	Superpixels	Pixel-by-Pixel Seconds	Superpixel Seconds	Speed Multiplier
1	Pelekane Bay	354,231	658	1,373,389.0	3442.5	398.9
2	East Kahoʻolawe	769,855	1232	2,984,804.8	8092.0	368.9
3	Hilo Bay	709,184	1036	2,749,577.3	5410.8	508.2
4	Māʻalaea	1,313,666	2256	5,093,214.4	23,147.0	220.0
5	South Molokaʻi	700,016	1063	2,714,032.0	5450.1	498.0

Water quality maps produced by both the pixel-by-pixel and the superpixel approach with a superpixel size of 600 matched qualitatively and quantitatively (Figures S1–S5). Horizontal transect profile plots showed that spatial patterns of magnitude were retained in the superpixel approach (Figure 2). Regressions between the pixel-by-pixel estimates and the superpixel estimates showed tight correspondence with R^2 values ranging from 0.78 to 0.95 for SPM, 0.83 to 0.99 for Chl-a, and 0.87 to 0.99 for CDOM (Figures 3–5; Table S1). All R^2 values were associated with extremely small *p*-values of less than 0.00001 largely due to the high number of samples (1000 for each example site). Importantly, superpixel-based modeling also appeared to greatly reduce the influence of pixel-level spectral noise and water surface variations on the output maps (Figures 2c–f and S1–S5).
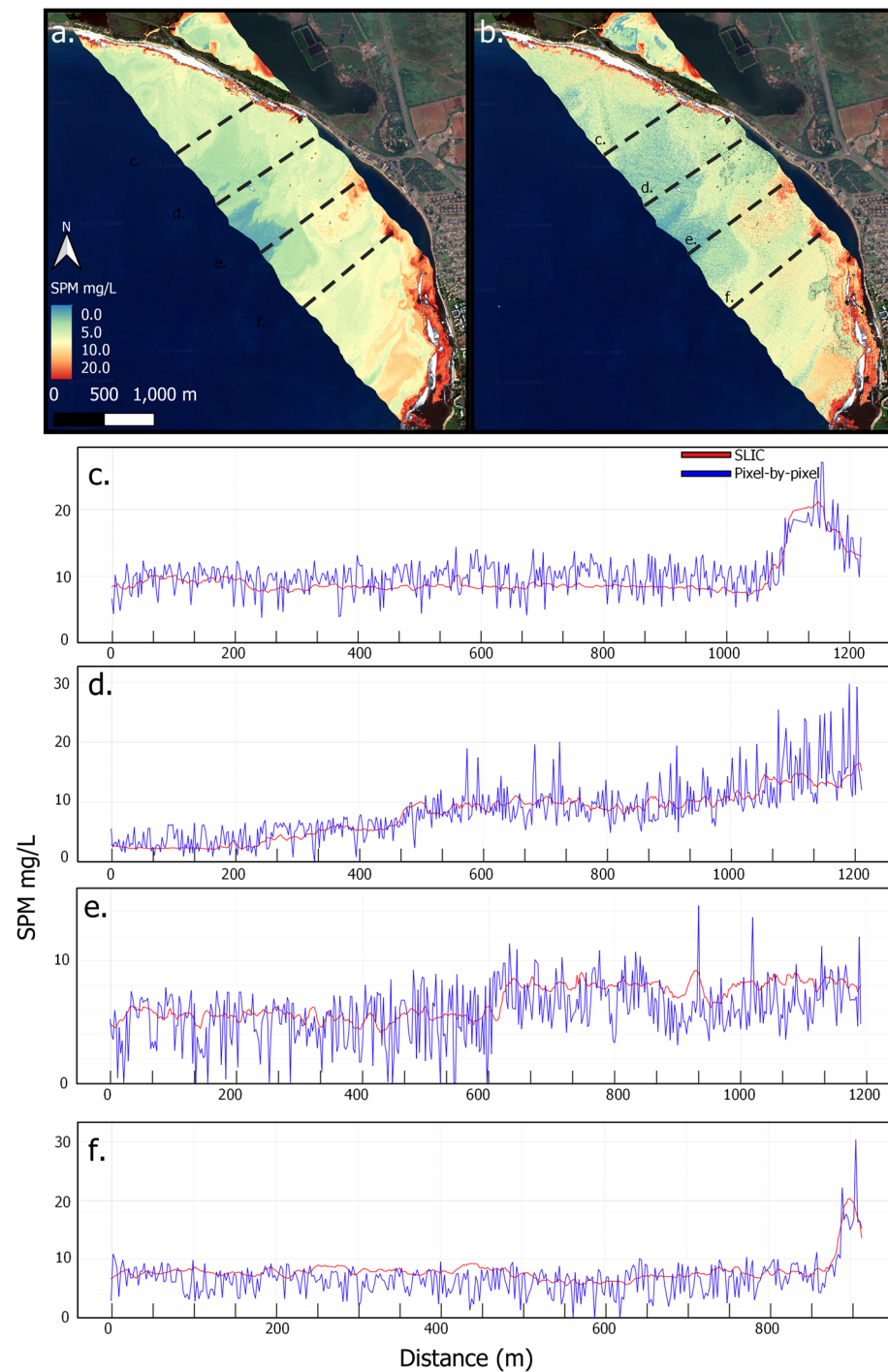
Figure 2. Transect profile plots of modeled values of suspended particulate matter (SPM) across four transects in the Mā'alaea site on Maui. Transect locations are shown on the output maps from the superpixel approach using a superpixel size of 600 pixels (2400 m² area) (**a**) and the pixel-by-pixel approach (**b**). Profiles for the superpixel map (red line) and the pixel-by-pixel map (blue line) visibly align in panels (**c–f**). The x-axes in the profile plots can be converted to pixel units by dividing by 2.
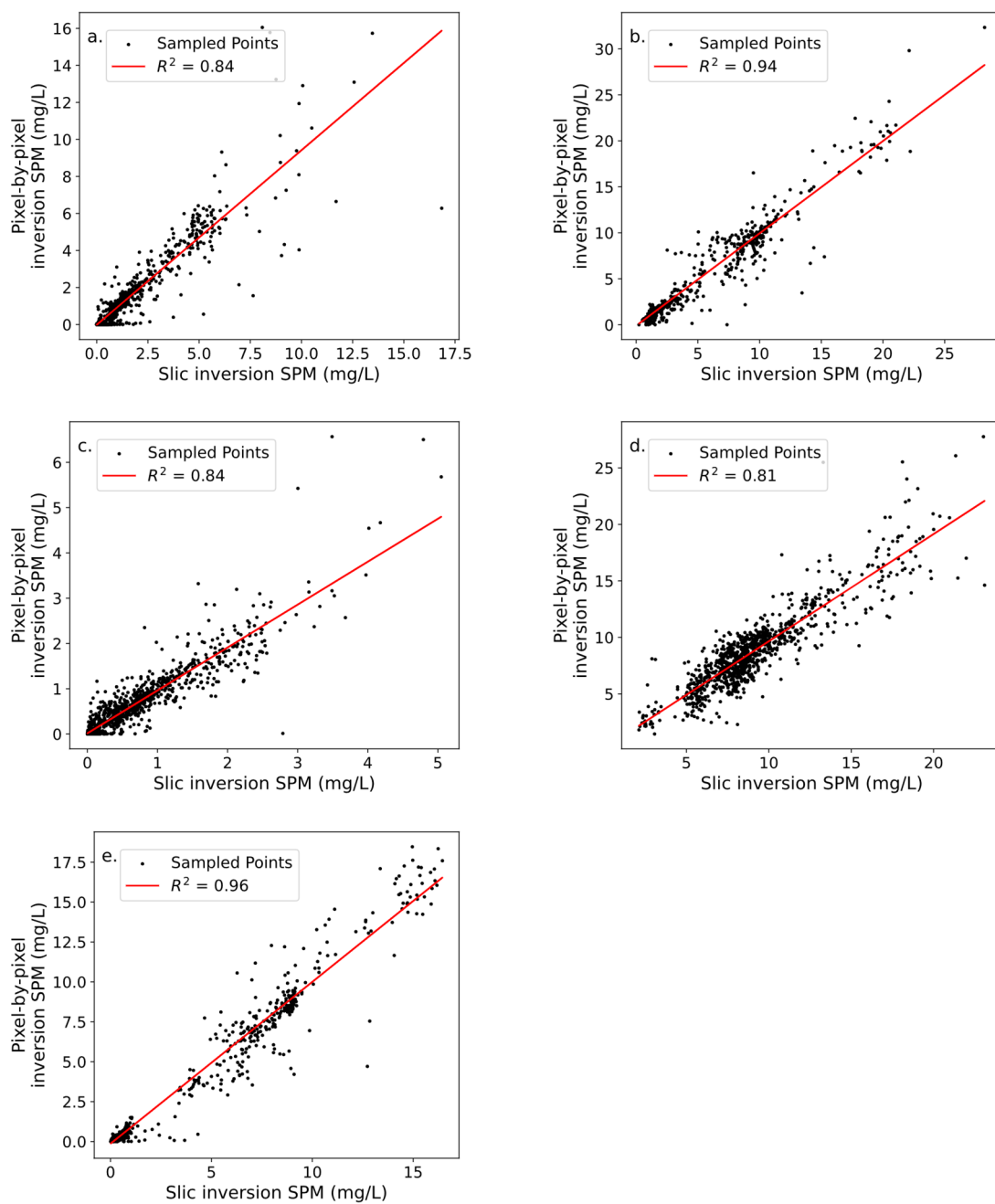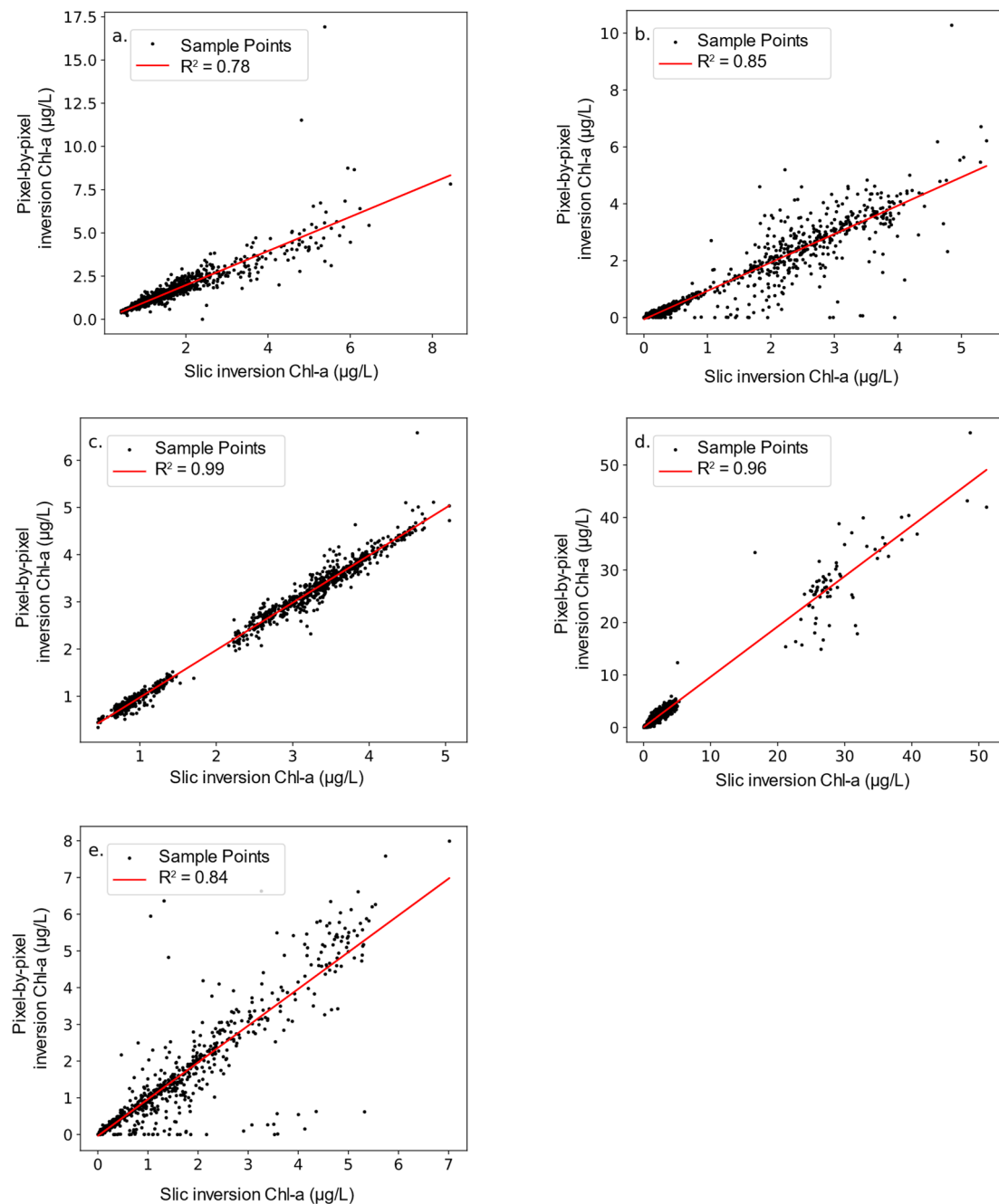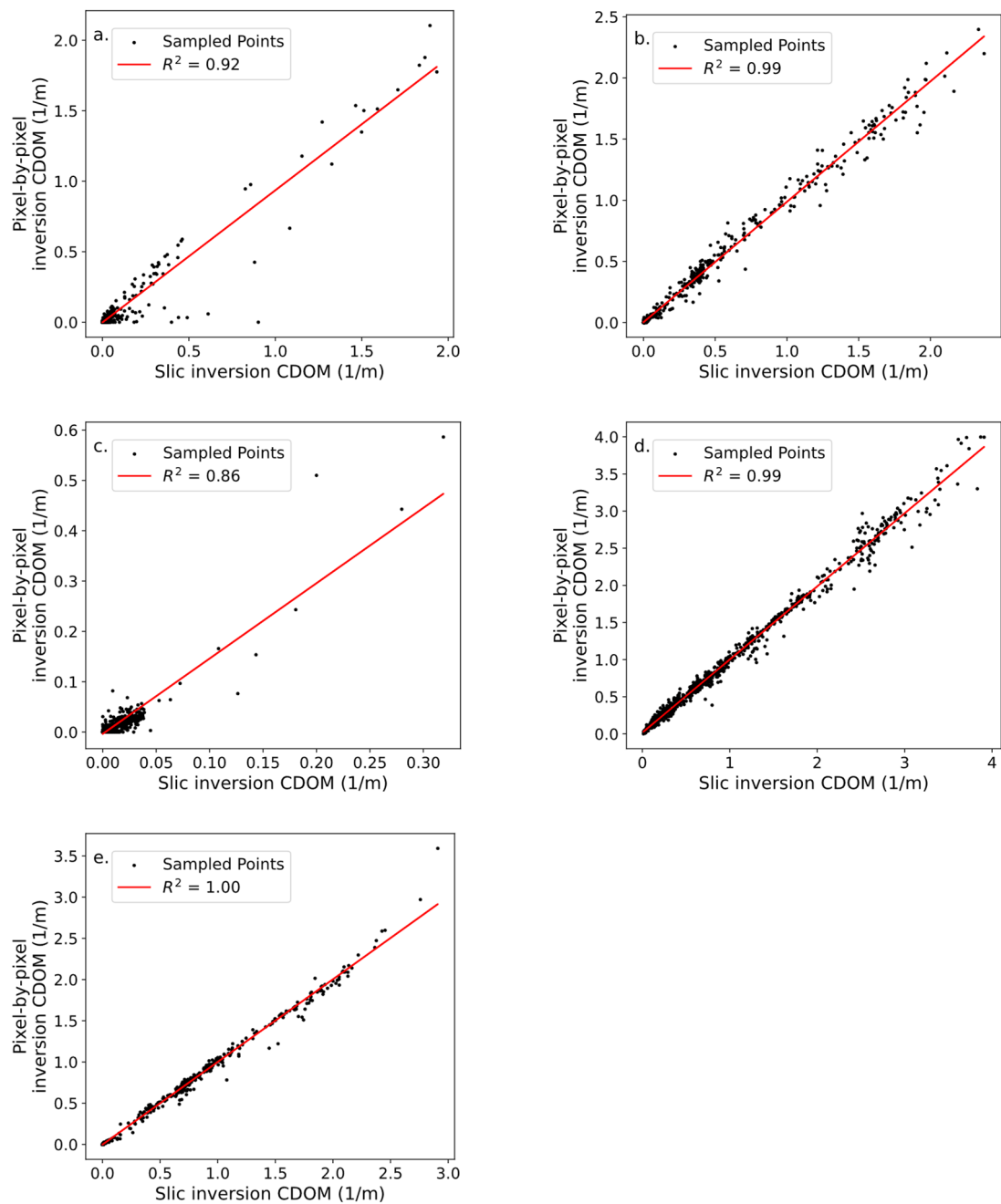
Figure 3. Regressions of suspended particulate matter (SPM) values from 1000 randomly selected matched pixels from the pixel-by-pixel approach and the superpixel approach for the (**a**) Pelekane Bay, (**b**) East Kahoʻolawe, (**c**) Hilo Bay, (**d**) Māʻalaea, and (**e**) South Molokaʻi example sites.

When we adjusted the superpixel size parameter across 13 settings between 50 and 5000 pixels, we found that, when averaged across the five example sites, accuracy generally decreased with increasing superpixel size (Figure 6a–c). However, the decrease was minimal in the case of SPM and Chl-a, as there was no clear pattern until sizes larger than 750 pixels were considered. Below this size, R^2 values varied around 0.84–0.88 for SPM and 0.86–0.93 for Chl-a, and RMSE values varied around 0.94–1.12 for SPM and 0.53–0.68 for Chl-a (Figure 6a,b). At sizes of 1000 pixels and above, there was a gradual decrease in R^2 down to 0.82 for SPM and 0.84 for Chl-a and a gradual increase in RMSE up to 1.24 for SPM and 0.72 for Chl-a. For CDOM, the decrease in accuracy was more consistent across the full range of superpixel sizes, with a more discernable decrease in R^2 from 0.98 to 0.89 from 50 to 5000 pixels in size and a parallel increase in RMSE from 0.034 to 0.055 along the

same gradient (Figure 6c). However, these patterns were less consistent when looking at individual sites, and we generally found that sites with a smaller range in an individual water quality parameter had higher variation in R^2 and RMSE for this parameter as superpixel size increased (Figure S6). Of note, in several cases across the five example sites and three water quality parameters, the maximal R^2 or minimal RMSE was found at mid-level superpixel sizes in the 250-to-1000-pixel range.
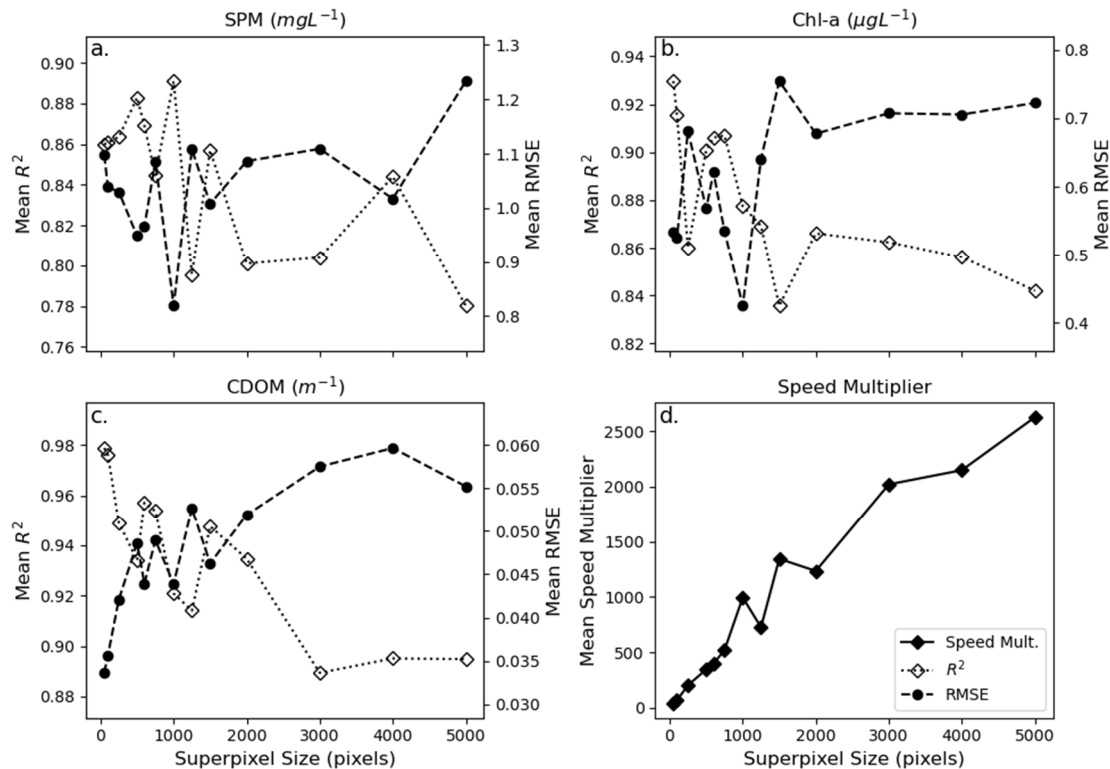

Figure 4. Regressions of chlorophyll-a (Chl-a) values from 1000 randomly selected matched pixels from the pixel-by-pixel approach and the superpixel approach for the (**a**) Pelekane Bay, (**b**) East Kahoʻolawe, (**c**) Hilo Bay, (**d**) Māʻalaea, and (**e**) South Molokaʻi example sites.

Figure 5. Regressions of colored dissolved organic matter (CDOM) values from 1000 randomly selected matched pixels from the pixel-by-pixel approach and the superpixel approach for the (**a**) Pelekane Bay, (**b**) East Kahoʻolawe, (**c**) Hilo Bay, (**d**) Māʻalaea, and (**e**) South Molokaʻi example sites. The sites with a larger range of CDOM have higher R^2 values, as shown in plot legends.

The assessment of variation within clusters of the output maps from the pixel-by-pixel approach again showed that spatial variation differed between the water quality constituents and by example site. Pixel-level RMSE values, which depict the variation within the superpixel clusters, grew along with superpixel size for all sites and constituents (Figure 7a,c,e). In all cases, RMSE grew most rapidly for the smaller superpixel sizes less than 1000 pixels. In example site 1, Pelekane Bay, RMSE reached an asymptote by the size of 2000 pixels for all three constituents, though none of the other sites appeared to reach an asymptote. Low values of the proportion of variance explained by within-cluster error (SSE/SST ≤ ~0.5) were observed for the smaller cluster sizes across nearly all example

sites and constituents (Figure 7b,d,f). Small values indicate that values within superpixel clusters are more similar to each other than the mean cluster values are across the map, which implies that clustering is successfully capturing the spatial distribution of the water quality constituents. Values of SSE/SST were particularly high at two sites, Pelekane Bay and Hilo Bay, indicating that sharp changes in the constituent value occurred within individual clusters at these sites. For all sites, we observed a pattern of a sharper increase in SSE/SST for superpixel sizes of less than 1000, matching the RMSE results.

Figure 6. Mean R^2 (dotted line) and RMSE (dashed line) statistics across the five example sites from regressions between the pixel-by-pixel approach and the superpixel approach for (**a**) suspended particulate matter (SPM), (**b**) chlorophyll-a (Chl-a), and (**c**) colored dissolved organic matter (CDOM) estimates from the bio-optical inversion model across the different superpixel sizes: 50, 100, 250, 500, 600, 750, 1000, 1250, 1500, 2000, 3000, 4000, 5000. In the bottom right panel (**d**), the speed increase in the super pixel approach over the pixel-by-pixel approach is shown.

Compared to accuracy values, the speed increase in the superpixel approach over the pixel-by-pixel approach was clearly linear with increasing superpixel size (Figure 6d). This pattern resulted from the fact that superpixel cluster size was measured in pixels, and thus size directly impacted the number of reduced bio-optical model iterations. For the smallest superpixels of size 50, the superpixel approach was approximately 38 times faster on average than the pixel-by-pixel approach. For the largest superpixel size setting, the proposed approach was 2625 times faster. We found that our default superpixel size of 600 was a good trade-off between map accuracy and speed savings—the superpixel approach was 398 times faster, on average, across the sample sites, over the pixel-by-pixel approach. This was equivalent to 2.5 h versus 34.5 days of computation time on a single CPU core for superpixel and pixel-by-pixel approaches, respectively.
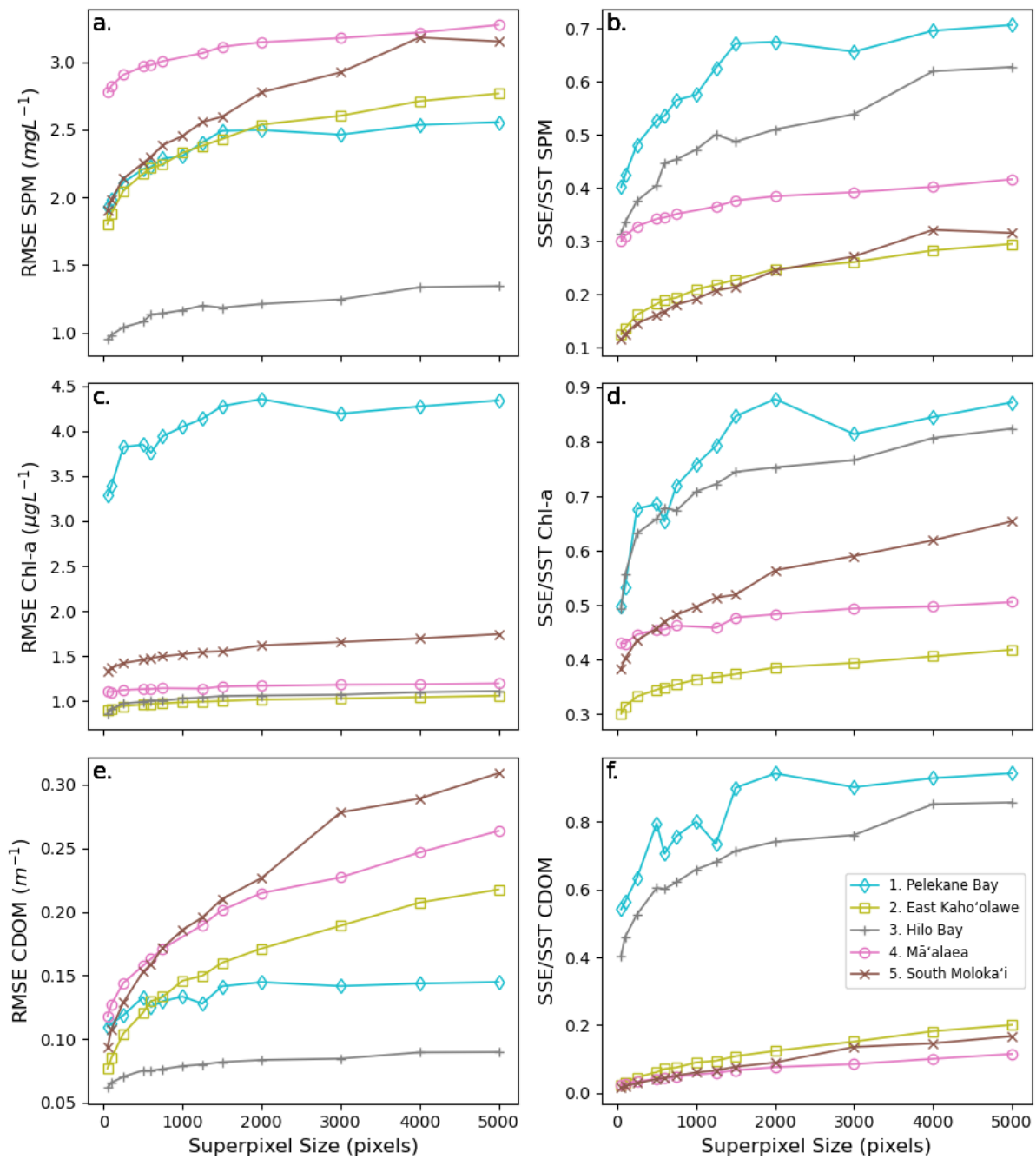
Figure 7. The analysis of variation in the pixel values in the water quality output from the pixel-by-pixel approach. Treating the superpixel clusters as a class variable, the left panels contain the RMSE, or the variation in pixel values within a cluster for (**a**) suspended particulate matter (SPM), (**c**) chlorophyll-a (Chl-a), and (**e**) colored dissolved organic matter (CDOM). The right panels show the proportion of total map variance explained by within-cluster errors (SSE/SST) for (**b**) SPM, (**d**) Chl-a, and (**f**) CDOM.

4. Discussion

We found that the time and computational resources needed for the creation of high-resolution water quality mapping from imaging spectroscopy data could be drastically reduced using a superpixel approach. While the spatial scale of the superpixels themselves strongly affected this reduction in resources as well as the accuracy of the rapid results in comparison to a simple pixel-by-pixel approach, acceptable levels of accuracy loss could be obtained with a fairly large speed benefit using a mid-range superpixel size

of approximately 600 pixels on a 2 m × 2 m resolution map. This finding suggests that the superpixel approach can be optimized to provide a practical solution for researchers and environmental managers who require timely and resource-efficient water quality mapping without significantly compromising the quality of the results. The total computation time needed to complete the superpixel approach across the sample sites was at the order of 2 h (though almost 7 were needed for the longest flight line at sample location 5). Thus, even with atmospheric correction, water quality maps could be computed from flight data within 24 h of flight, enabling what is considered near-real-time availability [11]. Eliminating the slow turnaround of remote-sensing-based water quality maps could increase uptake of this level of information by managers who have hesitated due to the minimal relevance of maps that take longer [31–33].

Beyond our results, similar performance and speed benefits have been found elsewhere when a superpixel approach has been applied to remote-sensing mapping projects. Researchers have long found significant speed and accuracy benefits in combining the spatial and spectral characteristics of individual pixels using clustering methods during classification and other thematic mapping projects [31–33]. For classification tasks in particular, a Geographic Object-Based Image Analysis (GEOBIA) was a dominant methodology in which superpixels were the object to be classified using shape and textural information from the individual pixels [34]. Given the shift to more deep learning methods in remote sensing, there has recently been strong interest in mixing superpixel input or post-processing with CNN modeling to capture the combined benefits of each of these tools [35–38]. However, with highly dimensional spectrometer data, it has generally been more common to use spectral unmixing approaches, and some work has focused on improving these methods with superpixel approaches [39,40]. Given this history, because of the computational needs of inversion modeling, applying superpixels to such an application was a natural next step. In fact, an example of such an application is the ISOFIT atmospheric correction software [22] used in the processing of our spectrometer data and which inspired our methodology used in this work. In this software, superpixels are used to reduce the number of slow atmospheric retrievals by taking advantage of the high mixture of gasses, vapors, and particles in the air. With the proven utility of superpixels across a wide range of mapping applications, there is little reason to second-guess the utility of incorporating them into our methodology.

Any approach using the agglomeration of spatial data to reduce computational requirements will necessitate a trade-off between speed and accuracy. Balancing these conflicting goals is a theme that occurs often across all applications of remote sensing in one form or another [41]. In this case, there are likely many scales at which the water quality parameters vary, and an optimal superpixel size would be related to underlying spatial autocorrelations resulting from physical processes controlling the mixing and transportation of the given constituents [42]. We sought to find a balancing point at which we could successfully capture this spatial variation across a site to a sufficient level and in a timespan that would be actionable. For this to be possible, we needed the superpixels to capture the range of values across and minimally blend across sharp edges. Allowing the SLIC clusters to vary in shape and follow such edges helped ensure that this edge blending was minimized (see Figures S1–S5); however, with larger superpixel sizes, variation within the superpixels became large enough to hinder the ability of our algorithm to maintain fidelity to the pixel-by-pixel maps (see Figure 6a–c). For SPM and Chl-a, we found that superpixel sizes of 750 pixels or less ($\leq 3000 \text{m}^2$) had fairly stable R^2 and RMSE values in regression models against the pixel-by-pixel approach across all sites. However, looking at the variation in mapped values within the various superpixels (Figure 7), we saw evidence that even the smallest cluster sizes were losing some spatial detail as RMSE and SSE/SST rapidly increased in these lower cluster sizes. This along with the jaggedness in the plots of R^2 and RMSE values (Figure 6a–c) below 750 pixels support that there were higher-frequency, smaller-magnitude patterns of spatial change in the water and some of the various superpixel size settings lined up with these frequencies. It is possible that poor

water surface conditions (glint, waves) seen in some of the pixel-by-pixel output maps (Figures 2c–f and S1–S5) operate at these smaller scales and might negatively affect the alignment of output maps from the pixel-by-pixel and superpixel approaches [43]. When testing this approach, we settled on a superpixel size of 600 pixels (2400 m^2) because we felt that this size sufficiently sped up inversion to a same-day scale but output maps also visually and quantitatively matched the range and distribution of the water quality constituent maps produced by the pixel-by-pixel approach. At this scale, there was some evidence of slight bias and softened edges (see Figure 2e,f), but these errors were within acceptable limits for a rapidly produced, actionable map.

Comparing our scaling results to previous studies, we found notable similarities and differences. Moses et al. (2016) analyzed data from spectrometers along with in situ instruments and looked at relationships between ground sampling distance (GSD) and the coefficient of variation (CV) of water properties within the specified sampling distance [42]. In most cases, CV rapidly increased with increasing GSD until a transitional point (tGSD), ranging from 75 to 600 m (~4400 to 282,700 m^2 circular pixel area), where the curve flattened. These results parallel those here, where both within-cluster variance as well as R^2 and RMSE values for the regressions between pixel-by-pixel and superpixel estimates deteriorated after superpixel size were large enough (~3000 m^2) for each parameter. Likewise, large transitional scales can be found in other work. Bisset et al. (2004) found that the largest GSD that could successfully quantify changes in spectral ocean color was 150 to 200 m (~17,600 to 31,400 m^2 area) within 5 km of shore [44]. Similarly, Jordan et al. (2023) found that R$_{rs}$ values from mobile radiometers had a limiting distance of detectable autocorrelation that ranged from 100 to 1000 m (7900 to 785,400 m^2 area) across several study sites [45]. Mahadevan and Campbell (2002) found evidence of even larger lags in semi-variograms of the distribution of chlorophyll in coarse MODIS data [46]. From these results, we believe that if we were to increase the maximum tested superpixel size beyond the 20,000 m^2 upper limit tested here, we would expect to see a continued loss of the ability to correctly interpolate the values to fill in the full resolution output maps and R^2 values would continue to decrease.

While this work was performed using the idea that the pixel-level maps were the true values, it is important to note that pixels represent only a random sample of a continuous surface with inherent errors and do not represent any real tangible square unit of area [47,48]. The pixel-by-pixel approach suffered from variations in modeled water quality stemming from fluctuations in water surface and spectral noise. Such patterns often occur in high-resolution mapping projects and are troublesome when mapping with a large number of spectral bands [43,49]. By running the inversions on superpixels, we took advantage of the fact that much of the pixel noise is random in nature and the averaging that took place within superpixels reduced the magnitude of this noise by a factor of $\sqrt{n}$, where n is the size of the superpixel in pixel units [50]. This likely reduced the number of iterations needed for optimization and the overall accuracy of the responses during the bio-optical inversion. Additionally, with superpixels in this study representing an approximate surface area of at least 200 m^2 and up to 20,000 m^2, the majority of water surface fluctuations from waves and other surface turbulence were effectively subdued in all of our maps from the superpixel approach. While the same could not be said about the effect of bottom surface constituency in shallower waters, slight improvement in this regard was also observed with the superpixel approach.

Given the above results, we believe this approach to be fairly transferable and scalable to other applications beyond water quality mapping. The methodology presented here is not dependent upon the particular bio-optical inversion model used to estimate parameters for the superpixel and pixel-by-pixel approaches. One caveat, however, in this work is that the water quality constituents were fairly well mixed even at the 2 m scale, which lends well to a superpixel approach. If applied to a situation where spatial patterning was more stochastic, i.e., too little spatial autocorrelation, then grouping neighboring pixels together would not be effective at capturing the range in values of interest. Also, superpixels may

not be appropriate if capturing the individual values with high accuracy is exceedingly more important than capturing the spatial trend [51]. In such a scenario, if there were a lot of sharp gradients within the water quality, one might consider modifying this approach to allow variable cluster sizes across the scene based on dynamic assessment of the input map. Similarly, for such situations, the PCA-based interpolation method might need to incorporate more components/eigenvectors to better capture the relationship between input and output values, perhaps even moving from a linear model to a nonlinear empirical model or a machine learning approach, but these would drastically increase the time needed to complete the interpolation step, reducing the realized gains of the superpixel approach. However, the efficient gains demonstrated in this study should be attainable in most thematic mapping situations where the value of interest is slow to compute from the input data but sufficiently correlated at scales larger than the input spatial resolution. In particular, while satellite-housed imaging spectrometers are currently only able to provide much coarser data than considered in this project, there is still reason to believe that this approach could benefit water-quality-mapping projects incorporating these data. Data volumes from satellite instruments that are always in motion have the potential to dwarf those of airborne campaigns, and such a reduction in computing resources would be even more beneficial and might enable mapping projects that would otherwise be insurmountable.

5. Conclusions

This study demonstrated the effectiveness of a superpixel approach for rapidly generating high-resolution water quality maps from imaging spectroscopy data. We found significant speed improvements with minimal loss of accuracy across the example sites. In addition, the superpixel approach visibly reduced the impacts of water surface undulations and spectral noise, potentially improving overall map quality and interpretability. The adjustable size of the superpixels should allow the methodology to be transferable to different settings and applications otherwise requiring computationally intensive modeling of each individual pixel. These dramatic speed improvements can make it feasible to process much larger datasets, potentially enabling regional- or global-scale water quality mapping from current and future high-resolution imaging spectrometers that meets both the latency and accuracy needs of water quality management. This should provide a valuable tool for environmental managers, researchers, and policymakers to address pressing water resource challenges. Future work could focus on further optimizing the method for specific applications, integrating it with other advanced processing techniques, or exploring its utility for additional environmental-monitoring tasks.

References

1. McDowell, R.W.; Noble, A.; Kittridge, M.; Ausseil, O.; Doscher, C.; Hamilton, D.P. Monitoring to Detect Changes in Water Quality to Meet Policy Objectives. *Sci. Rep.* **2024**, *14*, 1914. [CrossRef] [PubMed]
2. Gholizadeh, M.H.; Melesse, A.M.; Reddi, L. A Comprehensive Review on Water Quality Parameters Estimation Using Remote Sensing Techniques. *Sensors* **2016**, *16*, 1298. [CrossRef] [PubMed]
3. Ramadas, M.; Samantaray, A.K. Applications of Remote Sensing and GIS in Water Quality Monitoring and Remediation: A State-of-the-Art Review. In *Energy, Environment, and Sustainability*; Springer: Singapore, 2018; pp. 225–246, ISBN 9789811075506.
4. Yang, H.; Kong, J.; Hu, H.; Du, Y.; Gao, M.; Chen, F. A Review of Remote Sensing for Water Quality Retrieval: Progress and Challenges. *Remote Sens.* **2022**, *14*, 1770. [CrossRef]
5. Guo, Y.; Liu, C.; Ye, R.; Duan, Q. Advances on Water Quality Detection by UV-Vis Spectroscopy. *Appl. Sci.* **2020**, *10*, 6874. [CrossRef]
6. Giardino, C.; Brando, V.E.; Gege, P.; Pinnel, N.; Hochberg, E.; Knaeps, E.; Reusen, I.; Doerffer, R.; Bresciani, M.; Braga, F.; et al. Imaging Spectrometry of Inland and Coastal Waters: State of the Art, Achievements and Perspectives. *Surv. Geophys.* **2019**, *40*, 401–429. [CrossRef]
7. Matthews, M.W. A Current Review of Empirical Procedures of Remote Sensing in Inland and Near-Coastal Transitional Waters. *Int. J. Remote Sens.* **2011**, *32*, 6855–6899. [CrossRef]
8. Dekker, A.G.; Brando, V.E.; Anstee, J.M.; Pinnel, N.; Kutser, T.; Hoogenboom, E.J.; Peters, S.; Pasterkamp, R.; Vos, R.; Olbert, C.; et al. Imaging Spectrometry of Water. In *Imaging Spectrometry: Basic Principles and Prospective Applications*; van der Meer, F.D., Jong, S.M.D., Eds.; Springer: Dordrecht, The Netherlands, 2001; pp. 307–359, ISBN 9780306475788.
9. Botha, E.J.; Brando, V.E.; Anstee, J.M.; Dekker, A.G.; Sagar, S. Increased Spectral Resolution Enhances Coral Detection under Varying Water Conditions. *Remote Sens. Environ.* **2013**, *131*, 247–261. [CrossRef]
10. Odermatt, D.; Gitelson, A.; Brando, V.E.; Schaepman, M. Review of Constituent Retrieval in Optically Deep and Complex Waters from Satellite Imagery. *Remote Sens. Environ.* **2012**, *118*, 116–126. [CrossRef]
11. Schaeffer, B.A.; Schaeffer, K.G.; Keith, D.; Lunetta, R.S.; Conmy, R.; Gould, R.W. Barriers to Adopting Satellite Remote Sensing for Water Quality Management. *Int. J. Remote Sens.* **2013**, *34*, 7534–7544. [CrossRef]
12. Lee, Z.; Carder, K.L.; Mobley, C.D.; Steward, R.G.; Patch, J.S. Hyperspectral Remote Sensing for Shallow Waters: 2. Deriving Bottom Depths and Water Properties by Optimization. *Appl. Opt.* **1999**, *38*, 3831–3843. [CrossRef]
13. Albert, A.; Mobley, C. An Analytical Model for Subsurface Irradiance and Remote Sensing Reflectance in Deep and Shallow Case—2 Waters. *Opt. Express* **2003**, *11*, 2873–2890. [CrossRef]
14. Lesser, M.P.; Mobley, C.D. Bathymetry, Water Optical Properties, and Benthic Classification of Coral Reefs Using Hyperspectral Remote Sensing Imagery. *Coral Reefs* **2007**, *26*, 819–829. [CrossRef]
15. Gege, P. WASI-2D: A Software Tool for Regionally Optimized Analysis of Imaging Spectrometer Data from Deep and Shallow Waters. *Comput. Geosci.* **2014**, *62*, 208–215. [CrossRef]
16. Defoin-Platel, M.; Chami, M. How Ambiguous Is the Inverse Problem of Ocean Color in Coastal Waters? *J. Geophys. Res.* **2007**, *112*, C03004. [CrossRef]
17. Fell, F.; Fischer, J. Numerical Simulation of the Light Field in the Atmosphere–Ocean System Using the Matrix-Operator Method. *J. Quant. Spectrosc. Radiat. Transf.* **2001**, *69*, 351–388. [CrossRef]
18. Sawtell, R.W.; Anderson, R.; Tokars, R.; Lekki, J.D.; Shuchman, R.A.; Bosse, K.R.; Sayers, M.J. Real Time HABs Mapping Using NASA Glenn Hyperspectral Imager. *J. Great Lakes Res.* **2019**, *45*, 596–608. [CrossRef]
19. König, M.; Noel, P.; Hondula, K.; Jamalinia, E.; Dai, J.; Vaughn, N.; Asner, G. *CMLandOcean/Bio_optics*, Version v0.0.2; Zenodo: Tempe, AZ, USA, 2024.
20. Gege, P. Analytic Model for the Direct and Diffuse Components of Downwelling Spectral Irradiance in Water. *Appl. Opt.* **2012**, *51*, 1407–1419. [CrossRef]
21. Asner, G.P.; Knapp, D.E.; Boardman, J.; Green, R.O.; Kennedy-Bowdoin, T.; Eastwood, M.; Martin, R.E.; Anderson, C.; Field, C.B. Carnegie Airborne Observatory-2: Increasing Science Data Dimensionality via High-Fidelity Multi-Sensor Fusion. *Remote Sens. Environ.* **2012**, *124*, 454–465. [CrossRef]
22. Brodrick, P.; Erickson, A.; Olson, W.; Thompson, D.R.; Bohn, N.; Fahlen, J.E.; Shiklomanov, A.; Serbin, S.P.; Carmon, N.; Shinozu, Y.; et al. *Isofit/Isofit*, Version v2.9.8; Zenodo: Pasadena, CA, USA, 2023.
23. Thompson, D.R.; Natraj, V.; Green, R.O.; Helmlinger, M.C.; Gao, B.-C.; Eastwood, M.L. Optimal Estimation for Imaging Spectrometer Atmospheric Correction. *Remote Sens. Environ.* **2018**, *216*, 355–373. [CrossRef]
24. Feyisa, G.L.; Meilby, H.; Fensholt, R.; Proud, S.R. Automated Water Extraction Index: A New Technique for Surface Water Mapping Using Landsat Imagery. *Remote Sens. Environ.* **2014**, *140*, 23–35. [CrossRef]
25. Xu, H. Modification of Normalised Difference Water Index (NDWI) to Enhance Open Water Features in Remotely Sensed Imagery. *Int. J. Remote Sens.* **2006**, *27*, 3025–3033. [CrossRef]
26. Stutz, D.; Hermans, A.; Leibe, B. Superpixels: An Evaluation of the State-of-the-Art. *Comput. Vis. Image Underst.* **2018**, *166*, 1–27. [CrossRef]
27. Achanta, R.; Shaji, A.; Smith, K.; Lucchi, A.; Fua, P.; Süsstrunk, S. *Slic Superpixels*; École Polytechnique Fédérale de Lausanne: Lausanne, Switzerland, 2010.

28. van der Walt, S.; Schönberger, J.L.; Nunez-Iglesias, J.; Boulogne, F.; Warner, J.D.; Yager, N.; Gouillart, E.; Yu, T.; The Scikit-Image Contributors. Scikit-Image: Image Processing in Python. *PeerJ* **2014**, *2*, e453. [CrossRef]

29. Ding, X.; Gong, F.; Zhu, Q.; Li, J.; Wang, X.; Bai, R.; Xu, Y. Using Geostationary Satellite Ocean Color Data and Superpixel to Map the Diurnal Dynamics of Water Transparency in the Eastern China Seas. *Ecol. Indic.* **2022**, *142*, 109219. [CrossRef]

30. Jennewein, D.M.; Lee, J.; Kurtz, C.; Dizon, W.; Shaeffer, I.; Chapman, A.; Chiquete, A.; Burks, J.; Carlson, A.; Mason, N.; et al. The Sol Supercomputer at Arizona State University. In Proceedings of the Practice and Experience in Advanced Research Computing, Portland, OR, USA, 23–27 July 2023; ACM: New York, NY, USA, 2023.

31. Csillik, O. Fast Segmentation and Classification of Very High Resolution Remote Sensing Data Using SLIC Superpixels. *Remote Sens.* **2017**, *9*, 243. [CrossRef]

32. He, L.; Li, J.; Liu, C.; Li, S. Recent Advances on Spectral–Spatial Hyperspectral Image Classification: An Overview and New Guidelines. *IEEE Trans. Geosci. Remote Sens.* **2018**, *56*, 1579–1597. [CrossRef]

33. Cheng, G.; Han, J.; Lu, X. Remote Sensing Image Scene Classification: Benchmark and State of the Art. *Proc. IEEE Inst. Electr. Electron. Eng.* **2017**, *105*, 1865–1883. [CrossRef]

34. Blaschke, T.; Hay, G.J.; Kelly, M.; Lang, S.; Hofmann, P.; Addink, E.; Queiroz Feitosa, R.; van der Meer, F.; van der Werff, H.; van Coillie, F.; et al. Geographic Object-Based Image Analysis—Towards a New Paradigm. *ISPRS J. Photogramm. Remote Sens.* **2014**, *87*, 180–191. [CrossRef]

35. Yuan, X.; Shi, J.; Gu, L. A Review of Deep Learning Methods for Semantic Segmentation of Remote Sensing Imagery. *Expert Syst. Appl.* **2021**, *169*, 114417. [CrossRef]

36. Zhu, X.X.; Tuia, D.; Mou, L.; Xia, G.-S.; Zhang, L.; Xu, F.; Fraundorfer, F. Deep Learning in Remote Sensing: A Comprehensive Review and List of Resources. *IEEE Geosci. Remote Sens. Mag.* **2017**, *5*, 8–36. [CrossRef]

37. Mi, L.; Chen, Z. Superpixel-Enhanced Deep Neural Forest for Remote Sensing Image Semantic Segmentation. *ISPRS J. Photogramm. Remote Sens.* **2020**, *159*, 140–152. [CrossRef]

38. Yang, F.; Sun, Q.; Jin, H.; Zhou, Z. Superpixel Segmentation with Fully Convolutional Networks. In Proceedings of the Proceedings of the IEEE/CVF Conference on Computer Vision and Pattern Recognition (CVPR), Seattle, WA, USA, 13–19 June 2020; pp. 13964–13973. Available online: https://openaccess.thecvf.com (accessed on 1 June 2024).

39. Shi, C.; Wang, L. Incorporating Spatial Information in Spectral Unmixing: A Review. *Remote Sens. Environ.* **2014**, *149*, 70–87. [CrossRef]

40. Alkhatib, M.Q.; Velez-Reyes, M. Improved Spatial-Spectral Superpixel Hyperspectral Unmixing. *Remote Sens.* **2019**, *11*, 2374. [CrossRef]

41. Foody, G.M.; Sargent, I.M.J.; Atkinson, P.M.; Williams, J.W. Thematic Labelling from Hyperspectral Remotely Sensed Imagery: Trade-Offs in Image Properties. *Int. J. Remote Sens.* **2004**, *25*, 2337–2363. [CrossRef]

42. Moses, W.J.; Ackleson, S.G.; Hair, J.W.; Hostetler, C.A.; Miller, W.D. Spatial Scales of Optical Variability in the Coastal Ocean: Implications for Remote Sensing and *in Situ* Sampling. *J. Geophys. Res. Ocean.* **2016**, *121*, 4194–4208. [CrossRef]

43. Rasti, B.; Scheunders, P.; Ghamisi, P.; Licciardi, G.; Chanussot, J. Noise Reduction in Hyperspectral Imagery: Overview and Application. *Remote Sens.* **2018**, *10*, 482. [CrossRef]

44. Bissett, P.; Arnone, R.; Davis, C.; Dickey, T.; Dye, D.; Kohler, D.; Gould, R. From Meters to Kilometers: A Look at Ocean-Color Scales of Variability, Spatial Coherence, and the Need for Fine-Scale Remote Sensing in Coastal Ocean Optics. *Oceanography* **2004**, *17*, 32–43. [CrossRef]

45. Jordan, T.M.; Simis, S.G.H.; Selmes, N.; Sent, G.; Ienna, F.; Martinez-Vicente, V. Spatial Structure of in Situ Reflectance in Coastal and Inland Waters: Implications for Satellite Validation. *Front. Remote Sens.* **2023**, *4*, 1249521. [CrossRef]

46. Mahadevan, A.; Campbell, J.W. Biogeochemical Patchiness at the Sea Surface. *Geophys. Res. Lett.* **2002**, *29*, 32-1–32-4. [CrossRef]

47. Fisher, P. The Pixel: A Snare and a Delusion. *Int. J. Remote Sens.* **1997**, *18*, 679–685. [CrossRef]

48. Verhoeven, G. Pixels: So Basic but so Confusing. *AARGNEWS* **2018**, *56*, 28–33.

49. Jay, S.; Guillaume, M.; Minghelli, A.; Deville, Y.; Chami, M.; Lafrance, B.; Serfaty, V. Hyperspectral Remote Sensing of Shallow Waters: Considering Environmental Noise and Bottom Intra-Class Variability for Modeling and Inversion of Water Reflectance. *Remote Sens. Environ.* **2017**, *200*, 352–367. [CrossRef]

50. Thompson, D.R.; Mandrake, L.; Gilmore, M.S.; Castano, R. Superpixel Endmember Detection. *IEEE Trans. Geosci. Remote Sens.* **2010**, *48*, 4023–4033. [CrossRef]

51. Liao, N.; Guo, B.; Li, C.; Liu, H.; Zhang, C. BACA: Superpixel Segmentation with Boundary Awareness and Content Adaptation. *Remote Sens.* **2022**, *14*, 4572. [CrossRef]